Res Nondestr Eval (2001) 105–117 DOI: 10.1007/s00164-001-0013-y

Localization of a "Synthetic" Acoustic Emission Source on the Surface of a Fatigue Specimen

L. Gaul,[1] S. Hurlebaus,[1] L. J. Jacobs[2]

[1]Institute A of Mechanics, University of Stuttgart, Allmandring 5 b, 70550 Stuttgart, Germany
[2]School of Civil and Environmental Engineering, Georgia Institute of Technology, Atlanta, GA 30332-0355, USA

Abstract. The finite geometry of a laboratory specimen influences a measured acoustic emission waveform because of reflections, transmission, and mode conversion at the interface and boundaries of the specimen, thus making it difficult to determine the location of an acoustic emission (AE) source. The objective of this investigation is to develop a model experiment to identifiy the exact source location on the surface using "synthetic" AE signals. The AE event is generated by a short local thermal expansion. This expansion is produced by the absorption of a short laser pulse which provides a noncontact and broad-band generation of elastic waves. The signals are detected by a noncontact, broad-band, and high-fidelity sensor: a laser interferometer. The triangulation with several detectors is replaced by a single probe laser interferometer located at different coordinates under reproducible conditions. The recorded signals are analyzed by wavelet transform in order to determine the arrival times of waves for several frequency levels. These arrival times are used to quantify the location of the AE source in the surface as well as the velocity of the most dominant feature, the Rayleigh wave, and the time lag between the instant of the AE and the recording of the signal. The accuracy of the method is demonstrated by comparing the identified source location with the exact one.

1. Introduction

Elementary processes of deformation and fracture near a crack edge in a stressed body generate mechanical wave motions, which are collectively termed "acoustic emission" (AE). There is considerable interest in acoustic emission because it can be used to establish the geometric characteristics of cracks and to monitor the stability of existing cracks [1]. It is possible to monitor the tip velocity of a propagating crack if there is a monitoring system which localizes the acoustic emission source at different times.

There are a number of papers dealing with dynamic fracture. Freund [2] determined the pressure discontinuity radiating from a crack tip when the crack, which is initially at rest, begins to grow. Rose [3] gives explicit equations for the stress discontinuities radiated by a suddenly starting two-dimensional crack under tension, in an ideal elastic

Correspondence to: L. Gaul

body. These equations also give, with change in sign, the stress discontinuities radiated by a suddenly stopping crack, and, with a geometric deformation, those radiated by a three-dimensional crack. Achenbach and Harris [1] examined the AE signals from a semi-infinite crack of arbitrary shape using the elastodynamic ray theory. Jacobs et al. [4] used a source model for tracking the AE signal from a damage event in an infinite body, that is, an actual crack propagation and arrest event. Their source model includes the effect of the location of the crack, crack orientation, and crack tip velocity. The propagation of these cracks strongly affects the stress field in the vicinity of the crack tip, causing stress waves to radiate into the body and on the crack surface.

Only a few of the papers consider the identification of a crack event by AE testing. Hurlebaus et al. [5] developed a transfer function in order to remove the geometric features of an AE signal generated and detected in a fatigue specimen. The transfer function is developed by dividing (in the frequency domain) the signal of a halfspace (geometryless specimen) by the signal of a specimen whose geometry is being characterized. Once the transfer function has been developed for a particular specimen, it can operate on an arbitrarily generated signal of the specimen. However, the described method fails if the source location of the previously obtained transfer function does not match the source location of the arbitrary signal. Therefore, it is necessary to localize the AE source in order to make the corresponding transfer function.

Gaul and Hurlebaus [6] presented a technique to identify the impact location on a plate by using wavelets. This method is now applied to AE signals in order to show how efficiently the developed technique can be transfered to other applications.

The first section summarizes the relevant relations of the wavelet transform, while the next section presents the application of the wavelet analysis to waves. Then, the experimental setup and procedure as well as the fatigue specimen are described. The AE signals which are obtained with the technique shown are then wavelet-transformed and the arrival times of the Rayleigh wave are determined for each sensor location and frequency level. Based on these data, the localization of the "synthetic" AE source is shown, as well as the determination of the velocity of the Rayleigh wave.

2. Wavelet Transform (WT)

The continuous wavelet transform of an arbitrary function $f(t)$ as given by Strang and Nguyen [7] is defined by

$$F_\Psi(a,b) = \frac{1}{\sqrt{a}} \int_{-\infty}^{\infty} f(t)\Psi\left(\frac{t-b}{a}\right) dt, \tag{1}$$

including the analyzing function

$$\Psi_{a,b}(t) = \frac{1}{\sqrt{a}}\,\Psi\left(\frac{t-b}{a}\right) \tag{2}$$

as wavelet functions, with the position variable b and the scale variable a. The scaling is a primary characteristic of the wavelet analysis. In this investigation the relation between

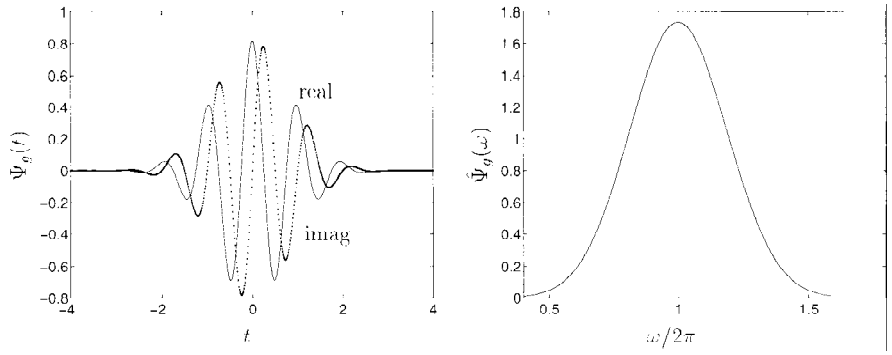

Fig. 1. Gabor function in the time (left) and in the frequency domain (right).

the scale variable a controlling dilatation and the frequency ω is $\omega = \omega_0/a$, where ω_0 is a positive constant. The function $\Psi(t)$ may be considered as a window function both in the time and frequency domain. The size of the time window is controlled by the translation, while the length of the frequency band is controlled by the dilation. It is possible to change the window size either in the time or in the frequency domain by controlling dilation and translation. This property of the WT is called multiresolution [8]. As has been suggested by Kishimoto et al. [9], the Gabor function is used as the analyzing wavelet because it provides a small window in the time as well as in the frequency domain. The Gabor function is defined by

$$\Psi_g(t) = \frac{1}{\sqrt[4]{\pi}}\sqrt{\frac{\omega_0}{\gamma}}\,\exp\left[-\frac{(\omega_0/\gamma)^2}{2}t^2 + i\omega_0 t\right]. \tag{3}$$

Following [9], the positive constants γ and ω_0 are set as $\gamma = \pi\sqrt{2/\ln 2}$ and $\omega_0 = 2\pi$, respectively. This Gabor function can be assumed as a complex sinusoidal function with a Gaussian window as shown in Fig. 1.

Using Parseval's theorem [7], the WT can be rearranged as

$$F_\Psi(a,b) = \frac{\sqrt{a}}{2\pi}\int_{-\infty}^{\infty}\hat{f}(\omega)e^{ib\omega}\,\overline{\hat{\Psi}(a\omega)}\,d\omega, \tag{4}$$

where

$$\hat{f}(\omega) = \int_{-\infty}^{\infty} f(t)e^{-i\omega t}\,dt, \tag{5}$$

is the Fourier transform of the function $f(t)$. The Gabor function in the frequency domain can be expressed by

$$\hat{\Psi}_g(\omega) = \frac{2\pi}{\sqrt[4]{\pi}}\sqrt{\frac{\gamma}{\omega_0}}\,\exp\left[-\frac{(\gamma/\omega_0)^2}{2}(\omega-\omega_0)^2\right]. \tag{6}$$

The advantage of the WT is that it provides high resolution in time as well as in the frequency domain. The reason for this as opposed to the short-time Fourier transform (STFT) is the selected time window, which is of variable size for all frequencies.

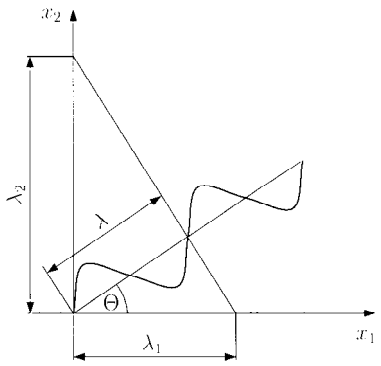

Fig. 2. Wave propagation in a plane.

3. Wavelet Analysis of Waves

It is important to know the relation between wave propagation and the wavelet analysis in order to determine the arrival times of waves. In general, a wave propagating in a plane can be specified by the wavelength λ and the angle Θ between the x_1 axes and the propagation direction. Hence, one can obtain the apparent wavelength in the x_1 and x_2 direction respectively, by $\lambda_1 = \lambda/\cos\,\Theta$ and $\lambda_2 = \lambda/\sin\,\Theta$ (Fig. 2).

The superposition of two waves traveling in a plane with the same amplitude and with frequencies ω_1 and ω_2, respectively, is given by

$$u(x_1, x_2, t) = e^{i(\omega_1 t - k_{11}x_1 - k_{12}x_2)} + e^{i(\omega_2 t - k_{21}x_1 - k_{22}x_2)}, \tag{7}$$

where k_{ji} are wave numbers corresponding to the frequency ω_j and to the coordinate x_i. In general, the wavenumber is defined as $k = 2\pi/\lambda$. Applying this definition to waves traveling in the same direction leads to the wavenumbers $k_{j1} = k_j \cos\,\Theta$ and $k_{j2} = k_j \sin\,\Theta$ and therefore the wave equation is expressed as

$$u(x_1, x_2, t) = e^{i(\omega_1 t - k_1 \cos\,\Theta x_1 - k_1 \sin\,\Theta x_2)} + e^{i(\omega_2 t - k_2 \cos\,\Theta x_1 - k_2 \sin\,\Theta x_2)}. \tag{8}$$

Defining $k_c = (k_1 + k_2)/2$, $\omega_c = (\omega_1 + \omega_2)/2$, $\Delta k = (k_1 - k_2)/2$, and $\Delta\omega_c = (\omega_1 - \omega_2)/2$, the wave package is

$$u(x_1, x_2, t) = 2\cos\,(\Delta\omega t - \Delta k \cos\,\Theta x_1 - \Delta k \sin\,\Theta x_2) e^{i(\omega_c t - k_c \cos\,\Theta x_1 - k_c \sin\,\Theta x_2)}. \tag{9}$$

By Fourier transform and wavelet transform of $u(x_1, x_2, t)$, the following expression is obtained:

$$\begin{aligned} F(x_1, x_2, a, b) \;=\; & \sqrt{a}[e^{i(\omega_1 b - k_1 \cos\,\Theta x_1 - k_1 \sin\,\Theta x_2)} \overline{\hat{\Psi}(a\omega_1)} \\ & + e^{i(\omega_2 b - k_2 \cos\,\Theta x_1 - k_2 \sin\,\Theta x_2)} \overline{\hat{\Psi}(a\omega_2)}]. \end{aligned} \tag{10}$$

Multiplying the conjugate complex of $F(x_1, x_2, a, b)$ by $F(x_1, x_2, a, b)$ leads to the magnitude of the wavelet transform under the assumption that $\hat{\Psi}(\omega)$ is real:

$$\begin{aligned} |F(x_1, x_2, a, b)| \;=\; & \sqrt{a}[\hat{\Psi}(a\omega_1)^2 + \hat{\Psi}(a\omega_2)^2 + 2\hat{\Psi}(a\omega_1)\hat{\Psi}(a\omega_2) \\ & \times \cos(2\Delta\omega b - 2\Delta k \cos\,\Theta x_1 - 2\Delta k \sin\,\Theta x_2)]^{1/2} \end{aligned} \tag{11}$$

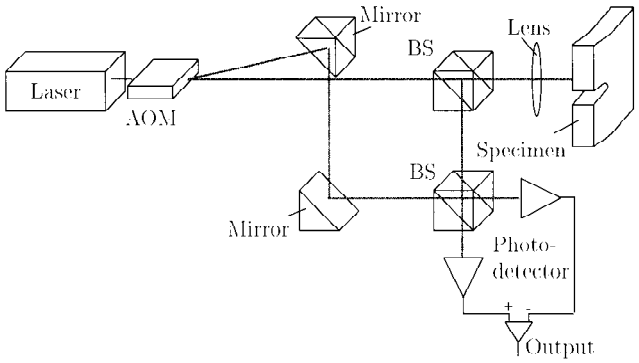

Fig. 3. Schematic arrangement of the heterodyne interferometer.

If Δk is small, then $k_1 \approx k_2$, $\omega_1 \approx \omega_2$, and $\hat{\Psi}(a\omega_1) \approx \hat{\Psi}(a\omega_2) \approx \hat{\Psi}(a\omega_c)$, and the magnitude of the wavelet transform is

$$|F(x_1, x_2, a, b)| \approx \sqrt{2a}|\hat{\Psi}(a\omega_c)| \times [1+2\cos(2\Delta\omega b - 2\Delta k \cos\Theta x_1 - 2\Delta k \sin\Theta x_2)]^{1/2}. \quad (12)$$

If

$$2\Delta\omega b - 2\Delta k \cos\Theta x_1 - 2\Delta k \sin\Theta x_2 = 0 \qquad \text{and} \qquad a = \frac{\omega_0}{\omega_c}, \quad (13)$$

the magnitude of the wavelet transform takes its maximum value. This is the case for

$$b = \frac{\Delta k}{\Delta\omega}(\cos\Theta x_1 + \sin\Theta x_2) = \frac{1}{c}(\cos\Theta x_1 + \sin\Theta x_2). \quad (14)$$

The maximum peak of the magnitude of the WT denotes the arrival time of the propagating wave with the group velocity c.

4. Experimental Setup and Procedure

Optical detection of AE is accomplished with a laser interferometer. The fundamentals of optical detection of ultrasonics are described in Sontag and Tam [10], who analyzed various optical techniques regarding their use for narrow acoustic pulse detection. Monchalin [11] as well as Wagner [12] presented reviews of various optical methods to detect ultrasound (bulk and surface waves) at the surface of opaque solids. Measurements in our paper were performed with a heterodyne interferometer. A detailed description of this interferometer can be found in [13]. Briefly, an acoustic-optic modulator (AOM) is used to split single-frequency light into two beams which differ in frequency (40 MHz in this application) (Fig. 3). These two beams are sent along two paths of the interferometer, one of which contains the sample being monitored. The two beams are recombined at a photodetector and produce a beat frequency of 40 MHz. Frequency shifts in light reflected from the sample surface result in proportional frequency shifts in the 40-MHz beat signal. As a result, the 40-MHz signal acts as a carrier that is demodulated in real time with

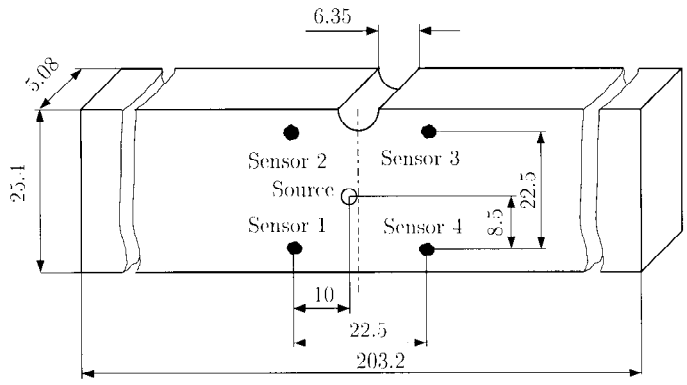

Fig. 4. Fatigue specimen and sensor positions (all dimensions in mm).

an FM discriminator to obtain the time-dependent surface velocity. The interferometer makes a high-fidelity, absolute measurement of surface velocity over a bandwidth of 10 MHz.

In 1963, White [14] introduced the concept of using transient heating to generate elastic waves. Lasers provide a convenient way of producing this transient heating because of their high power and their directionality. Laser generation of "synthetic" AE signals is accomplished using a Nd:YAG laser that emits a spatially Gaussian profile with a wavelength of 1,064 nm, a pulse duration of 15 ns, and a pulse energy of 6 mJ. The optical length of the pulse can be neglected compared to the duration of the recorded signals. Light from this pulse is used as a trigger that marks the instant when the acoustic wave is generated. There exist two different mechanisms for elastic wave generation: thermoelastic generation and ablation. The identification of these mechanisms and the estimation of the relative efficiencies are described by Aindow et al. [15]. In these experiments, the signal is created with an ablation mechanism as discussed in [16, 17]. In short, the physical principle behind ablation generation is that the incident electromagnetic energy from a Nd:YAG laser vaporizes a small amount of the surface material and the momentum transfer from this vaporization creates a force normal to the surface above the irradiated area. These transient forces generate Rayleigh surface waves, as well as body waves that propagate in a single broad lobe that is normal to the surface [18].

The fatigue crack specimen used for our work is made out of 2024 aluminum with dimensions as shown in Fig. 4. The specimen is polished with sandpaper, ending up with a finest grid size of 1,500, worked with steel wool, and then cleaned with acetone. The surface is polished to enhance the efficiency of optical detection; the more reflective the surface, the brighter is the reflected beam.

The experimental procedure consists of generating AE signals by a pulse laser and detection of these waveforms using a laser interferometer. Unfortunately, it is not possible to measure the waveforms simultaneously with just one single-probe interferometer; instead, the measurements have to be repeated, changing the location of the sensor in each experiment. Figure 5 shows the measured surface velocity at different detection locations. It is easily seen that the initial Rayleigh wave is the most dominant feature of

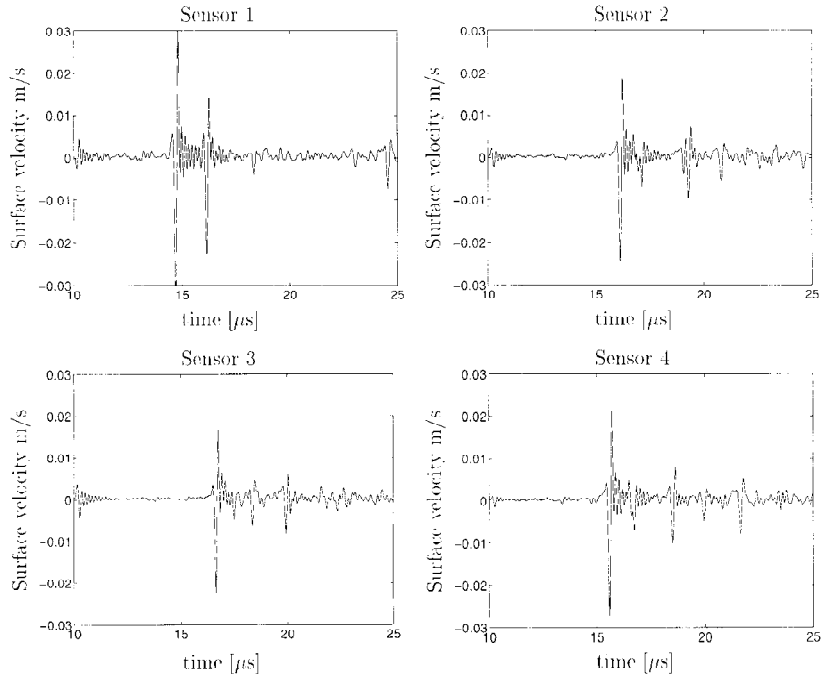

Fig. 5. Acoustic emission signals of sensor locations 1 to 4.

the waveform. However, there exist some other events which arise due to the multiple reflection of the Rayleigh wave as well as the body waves that propagate into the specimen and are reflected and mode-converted at the bottom surface.

5. Wavelet Transform of Acoustic Emission Signals

Once the experimental data are saved on a workstation, the signal processing procedure follows. It is important to window the signals before applying the Fourier transform. In this paper a Hanning window gives best results. However, the maximum of the Hanning window is at the half of the input sequence length of the signal, whereas the interesting part of the signal might not be at the same place as the maximum of the Hanning window. Therefore by using a common Hanning window, the interesting part of the signal may be reduced in amplitude whereas the less interesting part of the signal may be unchanged. To avoid this problem, zeros are added at the beginning or the end of the signal in order to “shift” the interesting part of the signal to the corresponding maximum of the Hanning window.

The signals are then transformed into the frequency domain using the fast Fourier transform (FFT). The discrete form of Eq. (4) leads to the wavelet domain of the four

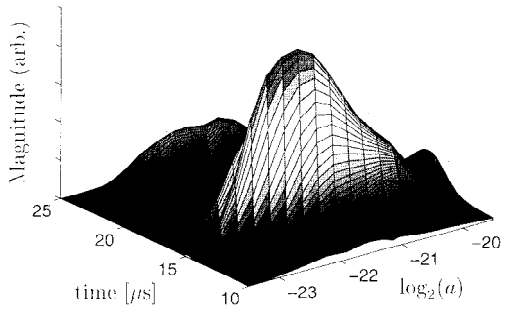

Fig. 6. 3-D plot of the wavelet transform.

signals. The parameters used in this transform are

$$a = 2^{m/4} \qquad \text{and} \qquad b = n\,\Delta t, \tag{15}$$

where m and n are integers. Newland [19] suggested the use of the wavelet transform starting in the time domain, transforming into the frequency domain, and finally transforming into the wavelet domain. This is preferred against direct transformation of the time-domain signal into the wavelet domain as shown in Eq. (1). The advantage is a savings in computational time by about two orders of magnitude. Figure 6 is the 3-D plot of the magnitude of the wavelet level at sensor location 1. The maximum of the plot can be easily seen, which indicates the arrival time of the flexural wave. Figure 7 shows the contour plot of the time–frequency analysis using the WT for each sensor signal.

6. Determining the Location of the AE Source, Time Lag, and Rayleigh Wave Velocity

In this section, the location of the AE source in the surface and the velocity of the Rayleigh wave are determined from the time–frequency analysis. As has been shown in Section 3, the maximum of the magnitude of the wavelet transform denotes the arrival time of the wave with velocity c. In order to get the arrival times, the maximum of the magnitude of the WT has to be determined for each frequency scale (Fig. 8). It is obvious that the incident waves are larger in amplitude than the reflected ones. This fact is used to obtain the maximum of the incident waves. Simply, the maximum of the wavelet transform denotes the arrival time of the incident Rayleigh wave. The arrival time of small values of $\log_2(a)$ (high frequencies) is the same as of large values of $\log_2(a)$ (low frequencies). This shows that the incident Rayleigh wave is of nondispersive nature.

Once the arrival times are known, one has to specify the coordinates of the location of the AE source, the time lag, and the Rayleigh wave velocity. The distances in the plane between sensor i and the location of the AE source is l_i. The corresponding arrival times are given by b_i and the unknown time lag is b_0. The unknown coordinates of the AE source in the surface are defined as x and y, respectively, while the side

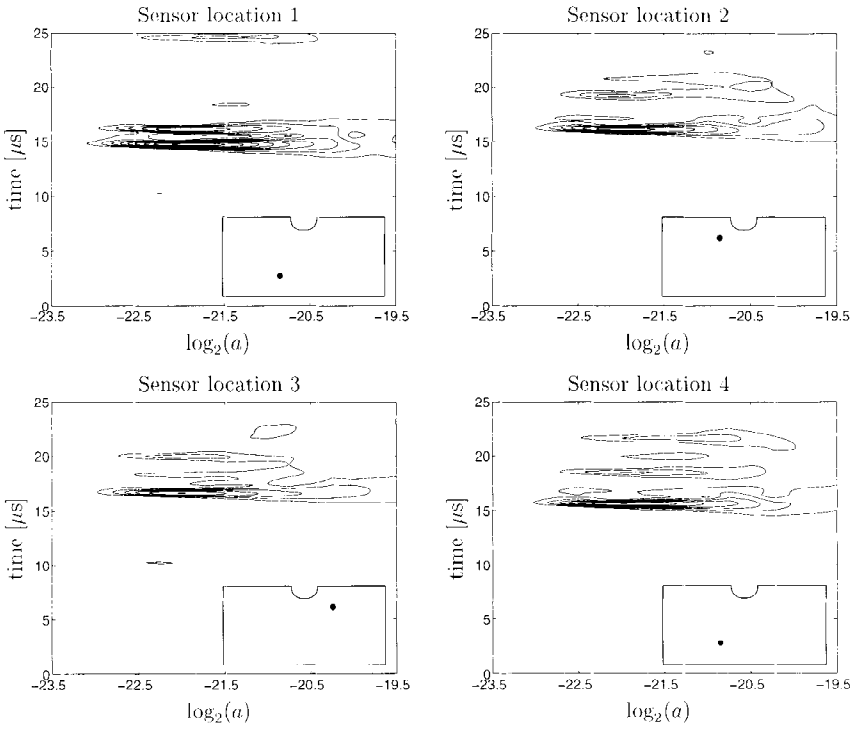

Fig. 7. Contour plots of the time–frequency analysis including the sensor locations.

length l of the squared configuration of the sensors is known. The relations among these magnitudes are

$$l_1 = \sqrt{x^2 + y^2}, \tag{16}$$

$$l_2 = \sqrt{x^2 + (l - y)^2}, \tag{17}$$

$$l_3 = \sqrt{(l - x)^2 + (l - y)^2}, \tag{18}$$

$$l_4 = \sqrt{(l - x)^2 + y^2}, \tag{19}$$

$$b_i(a) = b_0(a) + \frac{l_i}{c_R(a)} \qquad \text{for} \qquad i = 1, 2, 3, 4. \tag{20}$$

This is a system of eight equations for the unknowns b_0, c_R, x, y, l_1, l_2, l_3, and l_4. By rearranging, one obtains a system of four nonlinear equations:

$$b_1(a) = b_0(a) + \frac{\sqrt{x^2 + y^2}}{c_R(a)},$$

$$b_2(a) = b_0(a) + \frac{\sqrt{x^2 + (l - y)^2}}{c_R(a)},$$

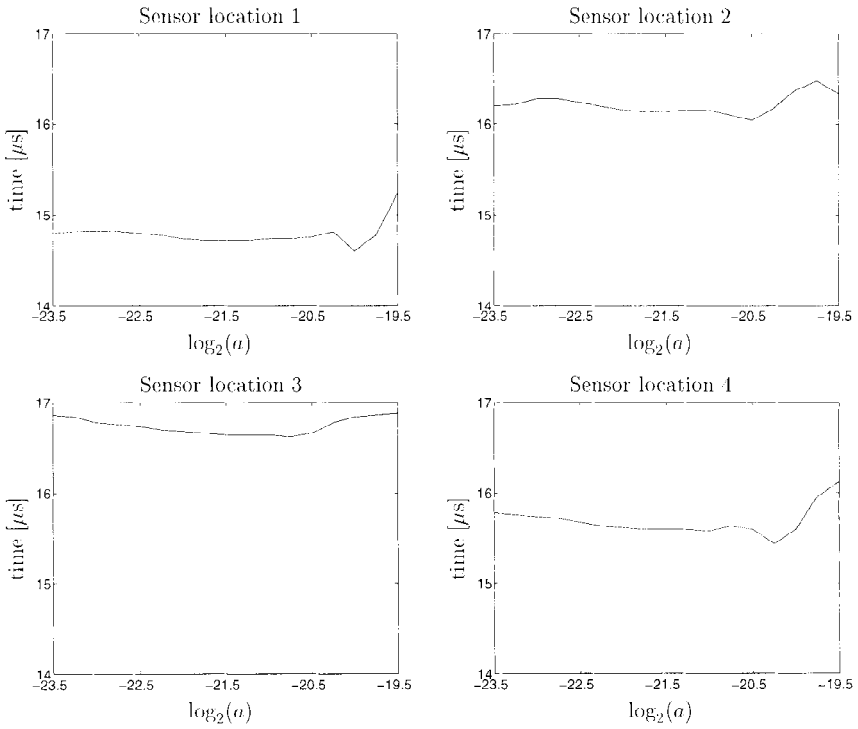

Fig. 8. Arrival times of the flexural waves of sensor 1 to 4.

$$b_3(a) = b_0(a) + \frac{\sqrt{(l-x)^2 + (l-y)^2}}{c_R(a)},$$
$$b_4(a) = b_0(a) + \frac{\sqrt{(l-x)^2 + y^2}}{c_R(a)}. \tag{21}$$

In practice, it is advantageous to solve this system of equations not analytically but by an optimization method. The adopted optimization method is described in more detail in [20]. Briefly, the set of equations (21) has to be reformulated into the form

$$\mathbf{f}(\mathbf{x}) = \mathbf{0}, \tag{22}$$

where $\mathbf{x}$ is the vector of the four unknown components $\mathbf{x} = (x, y, b_0, c_R)$. This procedure is based on the nonlinear least-squares optimization using the Gauss-Newton method, which is defined [20] as

$$\min \|\mathbf{J}(\mathbf{x_j})\mathbf{d_j} - \mathbf{f}(\mathbf{x_j})\|_2^2, \tag{23}$$

where $\mathbf{J}(\mathbf{x_j})$ is the Jacobian matrix of $\mathbf{f}(\mathbf{x_j})$ and $\mathbf{d_j}$ is the search direction. The search direction $\mathbf{d_j}$ is obtained for each major iteration, j, and can be used as part of a line search strategy to ensure that at each iteration expression (23) decreases.

For this optimization method an initial value $\mathbf{x_0}$ is necessary. One can get the initial value by a rough estimate of the Rayleigh wave velocity and then compute analytically

the initial values for the coordinates and the time lag. The estimation of the Rayleigh wave velocity is obtained by implementation of an analytical relation between the Rayleigh wave velocity and the material data. Graff [21] rederived the equations concerning the Rayleigh wave. He ended up with the equation for the phase velocity c_R of Rayleigh waves,

$$\left(2 - \frac{{c_R}^2}{{c_S}^2}\right)^2 - 4\sqrt{\left(1 - \frac{{c_R}^2}{{c_L}^2}\right)\left(1 - \frac{{c_R}^2}{{c_S}^2}\right)} = 0, \tag{24}$$

where c_L and c_S are the longitudinal and the shear wave velocity, respectively.

Denoting that the phase velocity is c_R (24) can be written as an equation for c_R/c_S, with Poisson's ratio ν as independent parameter, a good approximation of c_R/c_S can be written in terms of the Poisson's ratio:

$$\frac{c_R}{c_S} = \frac{0.87 + 1.12\nu}{1 + \nu}, \tag{25}$$

The shear-wave velocity for a semi-infinite medium depends on the modulus of elasticity E, density ρ, and Poisson's ratio ν:

$$c_S = \sqrt{\frac{1}{2(1+\nu)}\frac{E}{\rho}}. \tag{26}$$

By incorporating this information in the system of the four nonlinear equations of Eq. (21) and by eliminating the time lag b_0, one reduces the system to two nonlinear equations for the source coordinates x and y:

$$\begin{aligned} b_2(a) &= b_1(a) + \frac{\sqrt{x^2 + (l-y)^2}}{c_R(a)} - \frac{\sqrt{x^2 + y^2}}{c_R(a)}, \\ b_4(a) &= b_1(a) + \frac{\sqrt{(l-x)^2 + y^2}}{c_R(a)} - \frac{\sqrt{x^2 + y^2}}{c_R(a)}. \end{aligned} \tag{27}$$

In principle, this can be solved analytically. However, the results are not given here because the equations are still complicated.

By using the initial values on the optimization method one gets the coordinates of the location of the AE source, as well as the time lag and the velocity of the Rayleigh wave. Figure 9 presents the values of x and y for different frequency scales. By comparing these values with the actual values of the location of the AE source, all values of the coordinates of x and y which are obtained by the proposed approach are in the error range below 10%. However, averaging the identified values of x and y over the frequency scales considered leads to a coordinate in the x direction of 9.8 mm and a coordinate in the y direction of 8.5 mm. Compared to the actual values (x = 10 mm, y = 8.5 mm), these are reliable results. Moreover, Fig. 9 shows the time lag and the velocity of the Rayleigh wave for different frequency scales. The identified velocity is compared to the velocity obtained analytically. Again these velocities agree well in the frequency range considered because the analytical value of the Rayleigh wave velocity is taken as an initial value for the optimization procedure.

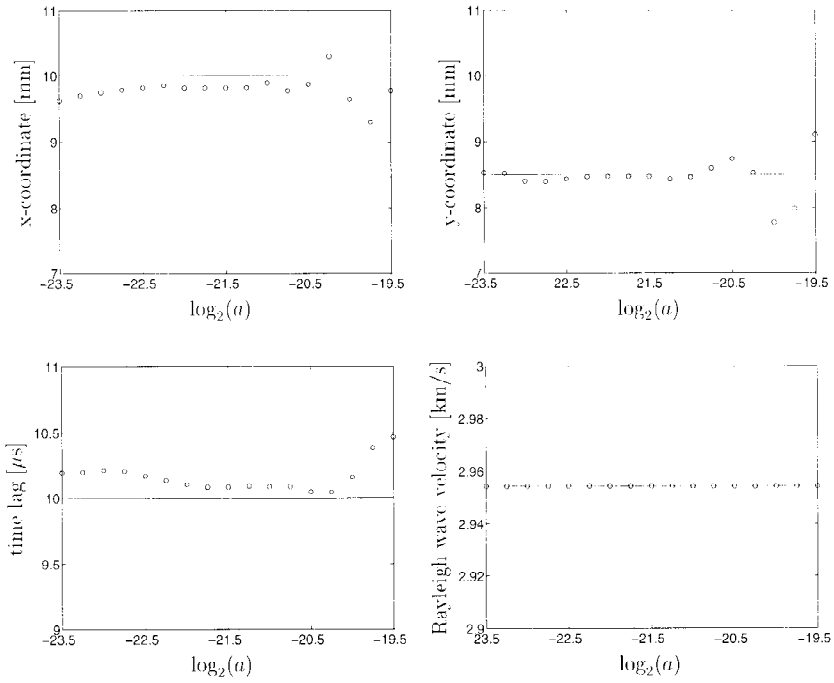

Fig. 9. Comparison of identified (circles) and theoretical data (solid lines) for coordinates of AE source, time lag, and Rayleigh wave velocity.

7. Conclusion

We presented a model experiment where we identify in a remote way the location of a "synthetic" laser-driven AE source on the surface. The technique developed is based on the wave propagation of acoustic waves in a fatigue specimen. The achieved accuracy of 2% is encouraging for the investigation of real AE sources. In that case the depth underneath the surface needs to be calculated as well. In addition, the lack of reproducibility of real AE sources means that one needs several detectors operating at the same time. For calibration of such experimental arrangement the described method is suited as well. This provides a means to make real AE comparable to deposited energies.

It is easy to extend this procedure to other types of waves such as body waves in order to localize the AE source inside a body. The advantages of the proposed method are the accuracy of the identified coordinates and that no exact knowledge of the material properties is required. A rough estimate of the material parameters is sufficient because an optimization algorithm is used to solve the nonlinear equations.

References

1. J. D. Achenbach and J. G. Harris. *J. Appl. Mech.* **46**:107–112 (1979).
2. L. B. Freund. *J. Appl. Mech.* **39**:601–602 (1972).

3. L. R. F. Rose. *Int. J. Fract*. **17**(1):45–60 (1981).
4. L. J. Jacobs, W. R. Scott, D. M. Granata, and M. J. Ryan. *J. Nondestr. Eval*. **10**(2):63–70 (1991).
5. S. Hurlebaus, L. J. Jacobs, and J. Jarzynski. *Nondestr. Test. Eval*. **14**:21–37 (1998).
6. L. Gaul and S. Hurlebaus. *Mech. Syst. Signal Process*. **12**:783–795 (1998).
7. G. Strang and T. Nguyen. *Wavelets and Filter Banks*, chap. 7. Wellesley-Cambridge Press, Wellesley, MA (1996).
8. Y. Wu and R. Du. *Mech. Syst. Signal Process*. **10**:29–53 (1996).
9. K. Kishimoto, H. Inoue, M. Hamada, and T. Shibuya. *J. Appl. Mech*. **62**:841–846 (1995).
10. H. Sontag and A. C. Tam. *IEEE Trans. Ultrason. Ferroelect. Freq. Control* **UFFC-33**(5):500–506 (1986).
11. J. P. Monchalin. *IEEE Trans. Ultrason. Ferroelect. Freq. Control* **UFFC-33**(5):485–499 (1986).
12. J. W. Wagner. *Phys. Acoustics* **19**:201–266 (1990).
13. D. A. Bruttomesso, L. J. Jacobs, and R. P. Costley. *J. Eng. Mech*. **119**(11):2303–2316 (1993).
14. R. M. White. *J. Appl. Phys*. **34**(12):3559–3567 (1963).
15. A. M. Aindow, R. J. Dewhurst, D. A. Hutchins, and S. B. Palmer. *J. Acoust. Soc. Am*. **69**(2):449–455 (1981).
16. D. A. Hutchins. *Phys. Acoust*. **18**:21–123 (1988).
17. C. B. Scruby and L. E. Drain. *Laser Ultrasonics*: *Techniques and Applications*. Adam Hilger, Philadelphia (1990).
18. H. M. Ledbetter and J. C. Moulder. *J. Acoust. Soc. Am*. **65**(3):840–842 (1979).
19. D. E. Newland. *Proc. DETC'*97. (DETC97/VIB-4135):1–12 (1997).
20. A. Grace. *MATLAB Optimization Toolbox*. MathWorks, Natick, MA (1992).
21. K. F. Graff. *Wave Motion in Elastic Solids*, p. 325. Dover, New York (1991).